

Entanglement analysis of isotropic spin-1 chains

Ronny Thomale¹, Stephan Rachel², B. Andrei Bernevig³, and Daniel P. Arovas⁴

¹ Institute for Theoretical Physics I, University of Würzburg, D-97074 Würzburg, Germany

² Institute for Theoretical Physics, TU Dresden, 01062 Dresden, Germany

³ Department of Physics, Princeton University, Princeton, NJ 08544, USA

⁴ Department of Physics, University of California at San Diego, La Jolla, California 92093, USA

Abstract. We investigate entanglement spectra of the $SO(3)$ bilinear-biquadratic spin-1 chain, a model with phases exhibiting spontaneous symmetry breaking (both translation and spin rotation), points of enlarged symmetry, and a symmetry-protected topological phase (the Haldane phase). Our analysis reveals how these hallmark features are manifested in the entanglement spectra, and highlights the versatility of entanglement spectra as a tool to study one-dimensional quantum systems via small finite size realizations.

1. Introduction

The notion of entanglement is central to quantum information theory, and has been applied with great success in the analysis of condensed matter systems [1]. Von Neumann entanglement entropy and its generalizations have been invoked in various contexts, including thermalization, diagnosis of topological phases, and properties of conformally invariant quantum systems. Beyond entanglement entropy, the full ‘entanglement spectrum’ of a system’s reduced density matrix ρ_A reveals much detailed information about the structure of its ground state [2]. In particular, block-diagonal structures in ρ_A derived from a many-body ground state projector $|\Psi_0\rangle\langle\Psi_0|$ may be exploited to analyze entanglement spectra as a function of quantum numbers associated with symmetries which are preserved by the entanglement cut. The notion of an ‘entanglement gap’ was established [2, 3] to suggest a separation of “relevant” low-lying entanglement levels from “spurious” low probability (high entanglement energy) levels. In some cases, such as the fractional quantum Hall effect and symmetry-protected topological phases (SPTs) [3, 4, 5, 6, 7, 8, 9, 10, 11, 12], the relevant low-lying levels have similarities to the energy levels of an edge Hamiltonian, although this line of reasoning is not universal [13].

While the task of connecting entanglement measures to physical observables is still at an early stage [14], the entanglement spectrum in particular has become a major

tool to investigate one-dimensional quantum many-body systems. On a qualitative level, this is due to the fact that entanglement spectra allow the reliable extraction of information far beyond that obtained from the entanglement entropy. For gapless 1-d systems, the entanglement spectral distribution is fully characterized by the central charge of the associated conformal field theory [15] which one could deduce from the entanglement entropy [16]. The entanglement spectrum, however, also determines the boson compactification radius associated with the operator content of the boundary CFT [17]. For gapped 1-d systems the entanglement spectrum can completely determine whether a system is topological or not, and provides a classification of such topological 1-d phases [11, 18].

In this article we investigate the finite size structure of the entanglement spectrum of the spin-1 bilinear biquadratic model for the spatial ground state bipartition of a 12 site realization, which will be defined in Section 2. For the ferromagnetic phase exhibiting spontaneous spin rotation symmetry breaking in the thermodynamic limit, the entanglement spectrum is calculated analytically and interpreted with respect to finite vs. infinite size entanglement in Section 3. In Section 4, the Uimin-Lai-Sutherland point of the quadrupolar phase is shown to exhibit an extensive number of zeroes in the reduced density matrix which we analytically trace back to its enlarged internal SU(3) symmetry. In Section 5, the dimerized phase with mod2 translation symmetry breaking is readily identified by the even-odd asymmetry of the ground state bipartition. At the negative biquadratic point, breaking of external symmetries, i.e. symmetry transformations involving the spatial coordinates such as translation, together with internal symmetry enhancement is shown to yield a rich entanglement structure. In the symmetry-protected topological Haldane phase discussed in Section 6, we find a correspondence between entanglement spectra and the low-energy spectrum of an open boundary Hamiltonian. We further employ the single mode approximation to obtain perturbative ground states around the Affleck-Kennedy-Lieb-Tasaki (AKLT) point, and show that it correctly yields the lowest-lying entanglement deformations away from AKLT. In Section 7, we conclude that entanglement spectra for finite size realizations constitute a highly efficient tool to understand the underlying structure of one-dimensional quantum many-body systems.

2. Model and ground state bipartition

We consider the bilinear biquadratic spin 1 chain given by

$$H = \sum_n \cos \theta \mathbf{S}_n \cdot \mathbf{S}_{n+1} + \sin \theta (\mathbf{S}_n \cdot \mathbf{S}_{n+1})^2, \quad (1)$$

where $\mathbf{S}_n = (S_n^x, S_n^y, S_n^z)$ are SO(3) spin operators $[S_n^\alpha, S_{n'}^\beta] = i\hbar \epsilon_{\alpha\beta\gamma} S_n^\gamma \delta_{nn'}$ and the angular parameter $0 \leq \theta < 2\pi$ specifies the sign and relative strength of the bilinear and biquadratic interactions. The phase diagram has been thoroughly investigated by numerical studies (Fig. 1). A ferromagnetic phase for $\pi/2 < \theta < 5\pi/4$ exhibits spin rotation symmetry breaking and is the only phase of (1) in which the ground state does

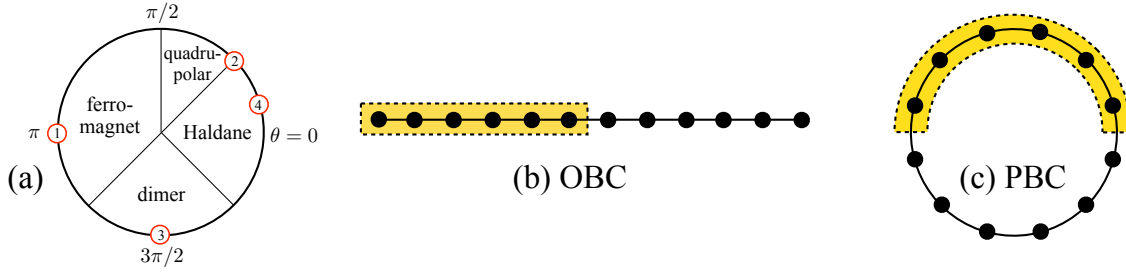


Figure 1. (a) Schematic phase diagram of the bilinear biquadratic model (1). The four points highlighted by red circles are of central interest in the following: (1) Heisenberg ferromagnet, (2) Uimin-Lai-Sutherland point, (3) the negative biquadratic model, and (4) the AKLT point. (b) Spatial bipartition of an open boundary 12 site chain resulting in one single cut. (c) Spatial bipartition of a periodic 12 site chain resulting in two cuts.

not reside in the singlet sector. The phase for $\pi/4 < \theta < \pi/2$ has been investigated numerically [19] and was found to be gapless with soft modes at $k = 0, 2\pi/3$ and $4\pi/3$, with the dominant quadrupolar correlations [20, 21]. At $\theta = \pi/4$, the quadrupolar phase terminates in the integrable Uimin-Lai-Sutherland point [22, 23, 24], which will be discussed further below. Throughout $-\pi/4 < \theta < \pi/4$, the ground state is a symmetry-protected topological phase identified by Haldane [25]. Anchored by the exact solution for a gapped valence bond solid at the AKLT point $\tan \theta = \frac{1}{4}$ [26], the persistence of the spin gap throughout the Haldane phase was investigated and confirmed by early large scale numerics [27, 28]. Finally, the dimerized phase for $5\pi/4 < \theta < 7\pi/4$ exhibits translation symmetry breaking as well as an associated dimerization gap, and is framed by the multicritical $SU(2)_2$ Takhtajan-Babujian point [29, 30, 31] to the Haldane phase and by the negative Uimin-Lai-Sutherland point to the ferromagnetic phase [32], where the latter transition point is challenging to resolve numerically because of the rapidly vanishing dimerization gap [33].

Consider a finite size realization of (1) for a given θ^* for N sites on open (OBC) or periodic (PBC) boundary conditions (Fig. 1). Because of finite size splitting, there will always be a unique ground state $|\Psi_0^{\theta^*}\rangle$ located in a Hilbert space $\mathcal{H} = \mathbf{1} \times \mathbf{1} \times \mathbf{1} \dots \times \mathbf{1} = \otimes_1^N \mathbf{1}$, where $\mathbf{1}$ represents the local spin-1 degree of freedom at a single site. According to the Schmidt decomposition with respect to a spatial bipartition, we split the Hilbert space into two regions A and B according to $\mathcal{H} = \mathcal{H}_A \times \mathcal{H}_B$, with the number of sites included in the regions given by $N_A + N_B = N$. From there, we define the reduced density matrix $\rho_A = \text{Tr}_B \rho$, where $\rho = |\Psi_0^{\theta^*}\rangle \langle \Psi_0^{\theta^*}|$, and Tr_B denotes a partial trace over all N_B sites. Following [2], this is associated with a Boltzmann factor of unit temperature $\rho_A = \exp(-H_A)$, where H_A denotes the entanglement Hamiltonian of region A . Depending on OBC or PBC, H_A mimics one or two cuts between region A and B (Fig. 1). The entanglement spectral levels will be denoted by $\xi = \text{spec}[H_A] = -\log(\text{spec}[\rho_A])$. (Note that aside from the real space partition introduced above, other cuts such as the momentum cut [34, 35, 36] or the rung cut [37, 38] have been advocated in the context

of low-dimensional spin systems.)

In the case of an isotropic spin chain as in (1), the block diagonal structure of ρ_A (and equivalently H_A) is fully determined by the spin representation of $|\Psi_0^{\theta*}\rangle$. If it is a singlet, i.e. $S^\alpha |\Psi_0^{\theta*}\rangle = 0$, it yields $[S_A^\alpha, \rho_A] = 0$, where $S_A^\alpha = \sum_{i \in A} S_i^\alpha$, $\alpha = x, y, z$, which gives the SO(3) multiplet structure of $[\mathbf{S}_A^2, \rho_A] = 0$ characterized by the eigenvalues $S_A(S_A + 1)$. If $|\Psi_0^{\theta*}\rangle$ is a spin multiplet such as in the ferromagnetic phase, it only holds $[S_A^z, \rho_A] = 0$ which gives a U(1) symmetry rather than a full SO(3) multiplet structure. In what follows, N_A and S_A characterize the subblocks of H_A . These quantum numbers allow to resolve manifestations of symmetry breaking, enhanced internal symmetry, and symmetry-protected character from the sole knowledge of finite size ground states of (1).

3. Ferromagnetic phase: spin rotation symmetry breaking

The ferromagnet extends to a wide region in (1), hosting at its boundaries at $\theta = \pi/2$ and $\theta = 5\pi/4$ two SU(3) symmetric ferromagnets. In many respects, the ferromagnet is the most trivial phase from the viewpoint of entanglement. In the thermodynamic limit where a magnetization axis is spontaneously chosen, the ground state is a single site product state and does not contain any entanglement. For finite size, however, the continuous spin symmetry of (1) cannot be broken, whereas the ground state $|\Psi_{\text{FM}}\rangle$ picks the largest available SO(3) representation. As such, $|\Psi_{\text{FM}}\rangle$ is uniquely defined independent of the specific choice of Hamiltonian in the ferromagnetic phase. As elaborated on in Section 2, $|\Psi_{\text{FM}}\rangle$ retains a U(1) symmetry in the entanglement spectrum ρ_A such that we can decompose it into according subblocks. We restrict the following discussion to $S^z \geq 0$ ($S_A^z \geq 0$) as the U(1) symmetry guarantees that subblocks with $-S^z$ ($-S_A^z$) are identical to those with S^z (S_A^z).

We begin with the ferromagnetic spin 1 ground state wave function. In the spin- $\frac{1}{2}$ case, the wavefunction has the most simple form, as all basis states acquire identical weight. For spin 1, we start by the subsector with maximum magnetization $S^z = N$, $|\Psi_{\text{FM}}^{S^z=N}\rangle = |\uparrow\uparrow \dots \uparrow\rangle$. From the knowledge of the multiplet structure, it must hold $S^2(S^-)^m |\Psi_{\text{FM}}^{S^z=S}\rangle = S(S+1)(S^-)^m |\Psi_{\text{FM}}^{S^z=S}\rangle \quad \forall m \in [0, \dots, 2S]$. This allows us to compute the relative weights of the different wave function partitions in S^z basis. With respect to $|\Psi_{\text{FM}}^{S^z=N}\rangle$, the spin 1 ferromagnetic wave function configurations acquire different relative weights due to different multiplicities of spin flip operators acting on the same site. For example, given $S^z = N - 2$, the basis is constructed by applying $S_i^- S_j^- |\uparrow\uparrow \dots \uparrow\rangle$, and configurations with $i \neq j$ acquire twice the weight of $i = j$ due to bosonic normalization.

Consider the bipartition of $|\Psi_{\text{FM}}\rangle$ in the $S^z = 0$ sector with $N_A = N/2$, as illustrated in Fig. 1. In the following, we assume the Schmidt basis of region A and B to be ordered according to decreasing relative weight. From the Schmidt decomposition, the (in general rectangular) entanglement matrix E_A can be defined as $\rho_A = E_A^T E_A$, which

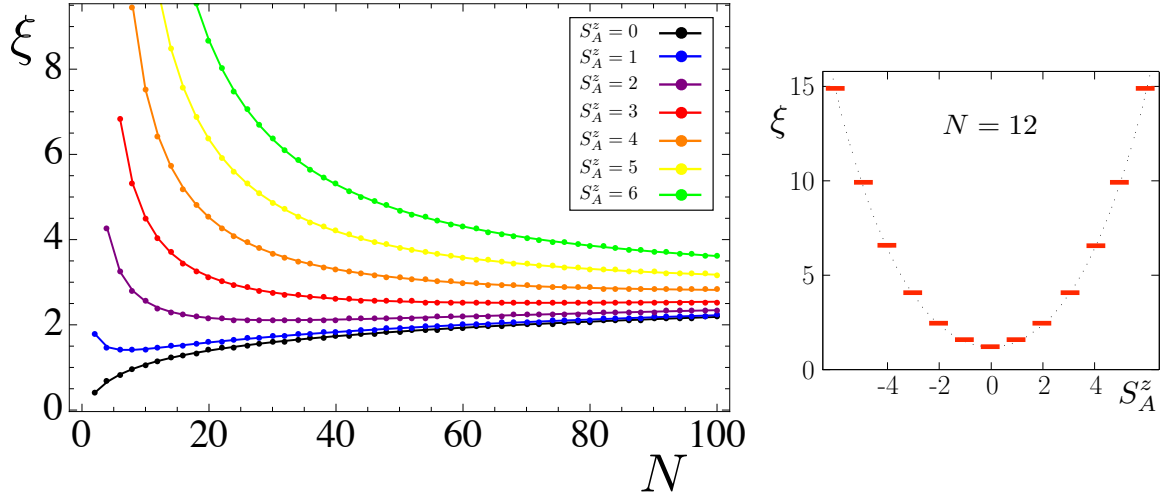


Figure 2. (Left) Analytical entanglement spectrum of the spin 1 ferromagnet as a function of total system size N for PBC. Each S_A^z sector contains one finite entanglement level. Different colors correspond to different S_A^z sectors as indicated in the legend. (Right) Example: ES vs. S_A^z for $N = 12$.

for $S_A^z = 0$, aside from global normalization, takes the form

$$E_A = \begin{pmatrix} 1 & 1/2 & 1/2 & \cdots & 1/4 & 1/4 & \cdots & (1/2)^m \\ 1/2 & 1/4 & 1/4 & \cdots & 1/8 & 1/8 & \cdots & (1/2)^{m+1} \\ 1/2 & 1/4 & 1/4 & \cdots & 1/8 & 1/8 & \cdots & (1/2)^{m+1} \\ \vdots & & & & & & & \vdots \end{pmatrix}. \quad (2)$$

One finds that the matrix E_A consists of several blocks with identical individual entries, the size of which being dictated by the number of basis states with the same relative weight. Determining the size of these blocks is given by the dimension of the S^z (S_A^z) subspaces of the Hilbert space for a given chain length N (N_A),

$$\dim \mathcal{H}(N, S^z) = \sum_{j=0}^{\lfloor (N-S^z)/2 \rfloor} \binom{N}{S^z + 2j} \binom{S^z + 2j}{j}, \quad (3)$$

where $\lfloor x \rfloor$ denotes the floor function. By construction, all columns (and rows) are linearly dependent, *i.e.*, E_A has rank 1 and the characteristic polynomial reads $P[\mu] = \mu^{N_A-1}(\mu - g)$ where $\mu = g$ is the only non-zero eigenvalue given by

$$g_{[N_A, S_A^z]} = \sum_{j=0}^{\lfloor (N_A - S_A^z)/2 \rfloor} \binom{N_A}{S_A^z + 2j} \binom{S_A^z + 2j}{j} 2^{-(2j + S_A^z)}. \quad (4)$$

Restoring the overall normalization of $|\Psi_{\text{FM}}\rangle$ leads to $\tilde{g}_{[N_A, S_A^z]} = g_{[N_A, S_A^z]} / \sqrt{\mathcal{N}_{[N, S_{\text{tot}}^z]}}$, where the norm is given by

$$\mathcal{N}_{[N, S_{\text{tot}}^z]}^2 = \sum_{j=0}^{\lfloor (N - S_{\text{tot}}^z)/2 \rfloor} \binom{N}{S_{\text{tot}}^z + 2j} \binom{S_{\text{tot}}^z + 2j}{j} 2^{-2j}. \quad (5)$$

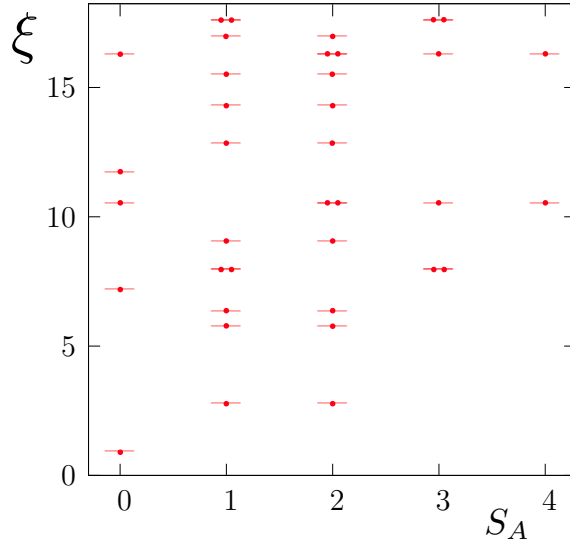


Figure 3. $(N, N_A) = (12, 6)$ entanglement spectrum (PBC) of the Uimin-Lai-Sutherland point decomposed into $\text{SO}(3)$ representations labeled by S_A . The enhanced $\text{SU}(3)$ symmetry becomes apparent from the eigenvalue degeneracies of different $\text{SO}(3)$ representations, such as a triplet and quintuplet forming an $\text{SU}(3)$ octet as the first entanglement energy above the lowest singlet level.

The non-zero eigenvalue of the reduced density matrix is then given by $|\tilde{g}_{[N_A, S_A^z]}|^2$, where the entanglement spectrum $\xi = -\log |\tilde{g}_{[N_A, S_A^z]}|^2$ is visualized for large system sizes in Fig. 2. In the right panel of Fig. 2, the same ES for $N = 12$ is plotted as a function of S_A^z . The parabolic form is a direct consequence of the binomial Hilbert space dimension for the different S_A^z sectors.

4. Quadrupolar phase: enhanced $\text{SU}(3)$ symmetry at $\theta = \pi/4$

Following numerical work [19], it was understood that the quadrupolar phase could be suitably characterized by the $\theta = \pi/4$ point. This is the Uimin-Lai-Sutherland (ULS) model, an integrable $\text{SU}(3)_1$ model with an exact solution of the Bethe *Ansatz* type [22, 23, 24]. At this point, the interaction between sites is, up to a constant, proportional to $-\text{P}_1(n, n+1)$, where P_1 is the projector onto total spin $J = 1$ for the neighboring sites. The $J = 1$ triplet is thus the ground state of the link, and the $J = 0$ singlet and $J = 2$ quintuplet combine to form a degenerate sextuplet. The Hamiltonian can then be mapped onto that of the antiferromagnetic $\text{SU}(3)$ Heisenberg chain in the fundamental representation, since $\mathbf{3} \otimes \mathbf{3} = \bar{\mathbf{3}} \oplus \mathbf{6}$. As known from the $\text{SU}(N)$ formulation of the Lieb-Schultz Mattis theorem [39], and consistent with the generalized $\text{SU}(N)$ Haldane-gap criterion [40], this model is gapless. Despite its solvability, from the viewpoint of numerical entanglement measures, it is still generally involved to extract the critical theory content for such models from finite size scaling [41].

The enhanced internal $\text{SU}(3)$ symmetry, however, can be readily derived (see

$$\underbrace{\square \times \square \times \dots \times \square}_{6 \times} = \begin{array}{|c|} \hline \square \\ \hline \square \\ \hline \square \\ \hline \end{array} + \dots + \begin{array}{|c|c|c|c|} \hline \square & \square & \square & \square \\ \hline \square & \square & \square & \square \\ \hline \end{array} + \begin{array}{|c|c|c|c|c|} \hline \square & \square & \square & \square & \square \\ \hline \square & \square & \square & \square & \square \\ \hline \end{array} + \begin{array}{|c|c|c|c|c|} \hline \square & \square & \square & \square & \square \\ \hline \square & \square & \square & \square & \square \\ \hline \end{array}$$

$N = 12, N_A = 6$

$5 \cdot \mathbf{35} \quad \mathbf{28}$
 $28 + 5 \cdot 35 = 203 \text{ zeros}$

Figure 4. Young tableaux decomposition of all SU(3) representations contained in the $N_A = 6$ Schmidt basis. The representations that do not comply with the SU(3) bipartition sum rule for an SU(3) singlet ground state are highlighted in orange, corresponding to ≥ 5 symmetrized blocks.

also [Appendix A](#)) and, because of its locality, manifests itself for any finite size realization. Along with the SU(3) singlet property of the ground state, this yields an SU(3) multiplet structure for ρ_A , where the representations of SU(2) arrange accordingly in the entanglement spectrum (Fig. 3). (Alternatively, one can directly adapt SU(3) Casimir operators J_3 and J_8 to label the individual blocks of ρ_A .) Aside from the exact SU(3) symmetry specific to the ULS point, the qualitative entanglement features carry over to the whole quadrupolar phase.

A notable aspect of ρ_A for finite size realizations of the ULS point is the observation of an extensive number of zeroes which are due to the enhanced SU(3) symmetry. To illustrate the latter for $N = 12$, note first that because of its singlet property, any ground state configuration should contain 4 green, blue, and red particles according to the notation in Fig. A1, which directly connects to 4 sites located in the state $S_i^z = -1, 0$, and 1, respectively. Considering now the Schmidt basis of region A (Fig. 1b), it trivially follows that any basis configuration will contribute a zero eigenvalue which would necessarily yield a total state configuration violating the SU(3) sum rule mentioned before. For $N = 12$ and $N_A = 6$, this corresponds to all configurations with 5 or 6 particles of one color in the Schmidt basis. Since all configurations form SU(3) multiplets, such configurations are interpreted as the seed states for the multiplets they belong to which are all disallowed, i.e. the total number of zeroes is given by the total dimensionality of the associated SU(3) representations. How many such representations, and hence how many zeroes of ρ_A , there are can be elegantly expressed in terms of SU(3) Young tableaux. For $N = 3 * n$, $n \in \mathbb{N}$, it corresponds to counting all representations with a number of symmetrized blocks that exceed n (Fig. 4). In our case, we have to consider $\mathbf{3}^{\otimes 6} = 5 \cdot \mathbf{1} \oplus 16 \cdot \mathbf{8} \oplus 10 \cdot \mathbf{10} \oplus 5 \cdot \overline{\mathbf{10}} \oplus 9 \cdot \mathbf{27} \oplus \mathbf{28} \oplus 5 \cdot \mathbf{35}$, and the total number of zeroes hence gives $5 \times 35 + 28 = 203$ in the ground state bipartition ρ_A due to SU(3) symmetry. Away from the ULS point, the zero modes of ρ_A for ULS become very small eigenvalues of ρ_A and hence yield entanglement levels at high ξ . It gives a generic explanation for the large amount of high entanglement energy levels in the quadrupolar phase. The argument of bipartition-induced zero mode representations carries over to analogous scenarios for SU(N) entanglement spectra.

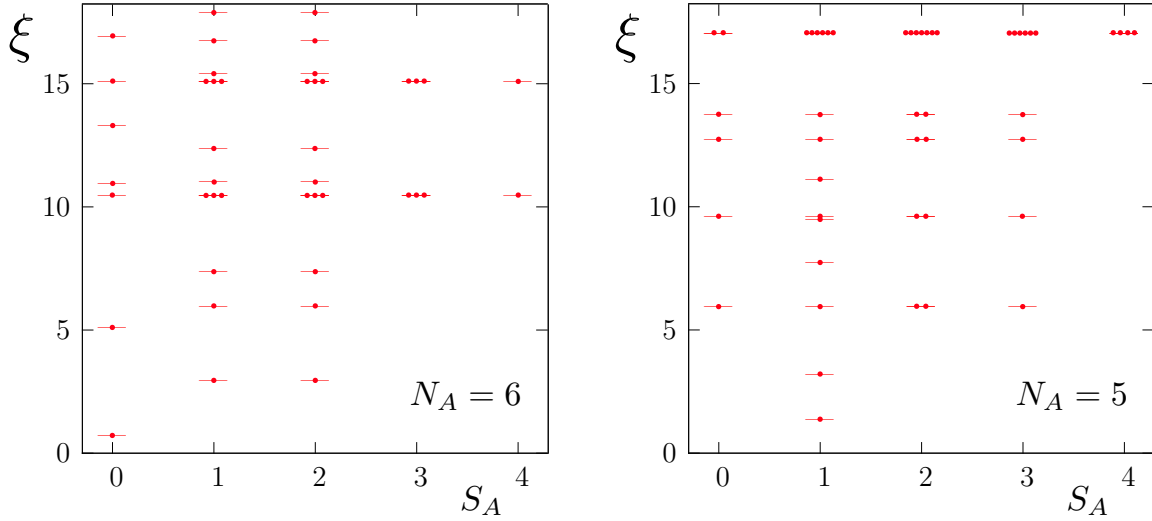


Figure 5. $N = 12$ entanglement cut for $N_A = 5$ and $N_A = 6$ for the dimerized $SU(3)$ point at $\theta = 3\pi/2$ for PBC. Aside from degeneracies between different S_A sectors dictated by enhanced $SU(3)$ symmetry, the low-lying entanglement spectrum of the gapped state switches between a singlet and triplet, which is reminiscent of translation symmetry breaking in the dimerized phase.

5. Dimerized phase: Translation symmetry breaking

5.1. $SU(3)$ dimerized point at $\theta = 3\pi/2$

As alluded to in [Appendix A](#), the model (1) for $\theta = 3\pi/2$ exhibits enhanced internal $SU(3)$ symmetry similar to the ULS point discussed in Section 4. Here, however, the Hilbert space relates to an alternating 3 and $\bar{3}$ representation. This has fundamental consequences on the very nature of the state. While it is still amenable to analytic solution, the state is not gapless but exhibits a gap along with translation symmetry breaking [42, 43], where the gap could be quantified by transfer matrix Bethe Ansatz [44] and allows to estimate a spin-spin correlation length of 21 sites. It is revealing how the joint appearance of enhanced $SU(3)$ and translational symmetry breaking manifests itself in the entanglement spectrum for small system sizes. To begin with, because of the $3 \times \bar{3}$ Hilbert space structure, there is only an $SU(3)$ sum rule for neighboring sites: in terms of $SO(3)$ spin configurations for an even number of lattice sites, it implies that one finds non-zero weights in the ground state wave function only for basis states composed of two-site sequences $[S_i^z, S_{i+1}^z] = [1, -1], [-1, 1],$ or $[0, 0]$. As such, these configuration constraints only act locally on consecutive sites, and do not trigger extensive zero modes as observed in Section 4.

5.2. Entanglement gap vs. energy gap

The onset of translational symmetry breaking can be detected e.g. by analyzing $(N, N_A) = (12, 5)$ and $(12, 6)$ (Fig. 5). For gapped spin chains, the correspondence

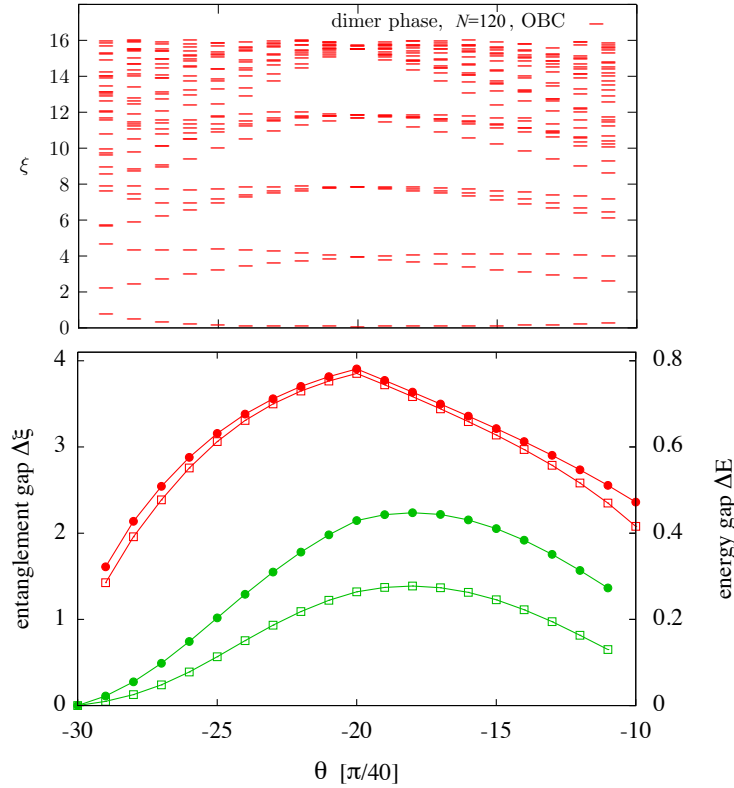


Figure 6. Upper panel: spectral flow of entanglement spectra in the dimerized phase obtained within DMRG. Lower panel: energy gap (green) in units of (1) and entanglement gap (red) in units of Boltzmann temperature for $N = 48$ and $N = 120$ (OBC). The entanglement gap maximum is shifted against the energy gap maximum.

between the entanglement spectrum and the open boundary Hamiltonian spectrum can be developed (see *e.g.* Ref. [45]). This is because the low-energy modes contributing to the entanglement Hamiltonian, as located at the *Schmidt boundary*, correspond to the low-energy modes located at the *physical boundary*. For entanglement spectra in the dimerized phase, the lowest lying singlet state seen for $N_A = 0 \bmod 2$ alternates with the lowest lying triplet state for $N_A = 1 \bmod 2$. Note that this is not trivially dictated by the Hilbert space structure, as any even or odd tensor product of $\text{SO}(3)$ representations contains singlets. Upon inspection, both low-energy spectra for $(N, N_A) = (12, 5)$ and $(12, 6)$, in terms of spectral structure and eigenvectors, correspond to an OBC $N = 5$ and $N = 6$ realization of (1). The even chain yields a lowest-lying dimerized singlet, while the lowest-lying odd chain state breaks a dimer singlet into a triplet state.

This spectral structure carries over to the entanglement spectrum of the whole dimer phase. For the $N_A = 6$ cut, an entanglement gap between the singlet state and the second lowest quintuplet state ($\theta > 3\pi/2$) or triplet state ($\theta < 3\pi/2$) can be defined (*cf.* Fig. 6), with a corresponding level crossing cusp at $\theta = 3\pi/2$ [46] (see also Appendix B). Interestingly, the energy gap shows a similar, but not identical behavior. As can be also supported by larger scale density matrix renormalization group (DMRG) calculations, the energy gap maximum does not match the entanglement gap

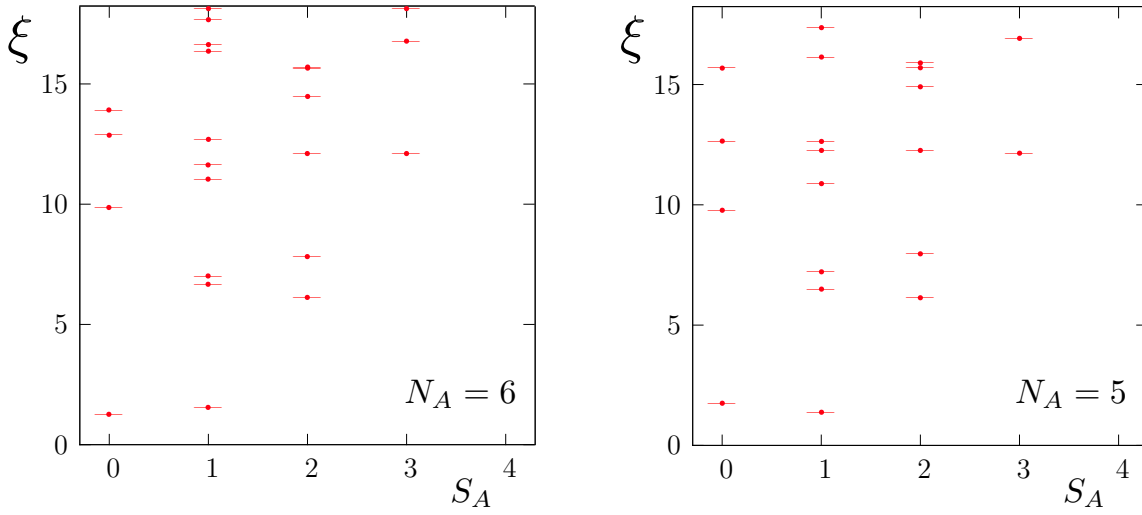


Figure 7. Entanglement spectrum for $(N, N_A) = (12, 6)$ and $(12, 5)$ in the Haldane phase at $\theta = \pi/20$ for PBC. The low energy spectrum is given by a triplet and a singlet separated from higher levels. The spectrum is similar to the corresponding Hamiltonian spectrum for open boundaries.

maximum (Fig. 6). It stresses once again that while certain universality features are shared between energy spectra and entanglement spectra in gapped phases, this does not extend to non-universal features such as gap maxima.

6. Symmetry-protected topological Haldane phase

The Haldane phase exhibits an energy gap without breaking of translation symmetry. The entanglement analysis shows no breaking of any other symmetry of (1). The correspondence between the entanglement spectrum and the OBC Hamiltonian spectrum can be studied already for small finite system size. Fig. 7 shows the entanglement spectrum for even and odd N_A . The general structure of the entanglement spectrum stays unchanged, in clear contrast to the analogous analysis for the dimerized phase in Fig. 5. A triplet and a singlet level appear to form a separated low-energy set from the rest of the energy spectrum, where the singlet (triplet) state is the lowest entanglement energy state for even (odd) N_A . This is identically found for the OBC Hamiltonian spectrum.

6.1. Entanglement gap vs. energy gap

The gap of the Haldane phase, and its entanglement Hamiltonian correspondence to OBC spectra derived from there, is identified as a Berry phase effect in integer spin chains [25] and characterized by the AKLT point where the gap can be calculated analytically [26]. The AKLT model has become the paradigmatic symmetry-protected topological phase in one dimension [11], where the OBC low-energy behavior is

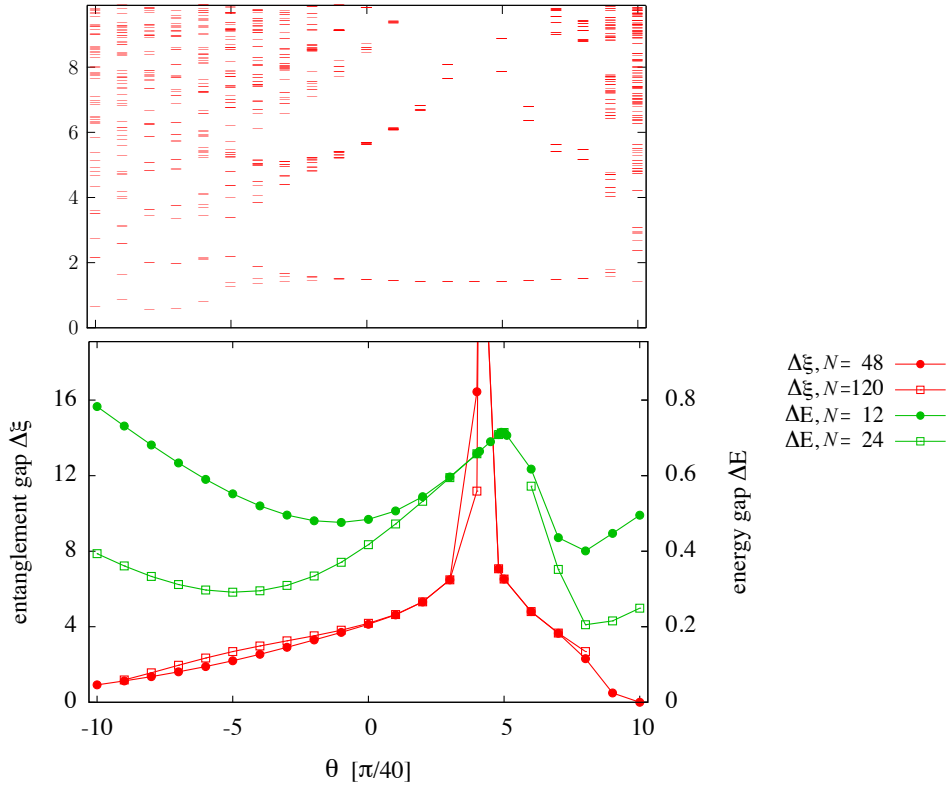


Figure 8. Upper panel: Entanglement spectral flow of the Haldane phase obtained within DMRG for $N = 48$ (PBC). Lower panel: Energy gap vs. entanglement gap for OBC. The proper investigation of the energy gap for large system sizes yields gap closure at $\pm\pi/4$ and a maximum energy-gap position shifted against the AKLT point [28].

characterized by one dangling spin- $\frac{1}{2}$ degree of freedom at each boundary. This likewise characterizes the low-energy entanglement spectrum, *i.e.*, the dangling spins form a triplet and a singlet which are separated from the other levels by an entanglement gap or energy gap, respectively (Appendix B). While the energy gap always stays finite, the entanglement gap becomes infinite at the AKLT point, where the ground state can be exactly characterized by a matrix product state with bond dimension $\mathcal{D} = 2$.

Fig. 8 depicts the entanglement spectral flow through the Haldane phase along with a comparison of energy gap vs. entanglement gap. From the AKLT point, branches of levels come down in entanglement energy and eventually close the entanglement gap towards the ULS point at $\pi/4$ and the Takhtajan-Babujian point at $-\pi/4$, respectively. The energy gap similarly closes at $\pm\pi/4$ as seen in finite size scaling, but exhibits a gap maximum shifted against the entanglement gap maximum at the AKLT point. (The observation from small finite size is confirmed by large scale calculations, see e.g. Ref. [28].) This is similar to the dimerized phase in Fig. 6.

6.2. Single mode approximation

Our starting point is the AKLT Hamiltonian plus the Heisenberg term as a small perturbation,

$$H = H_{\text{AKLT}} + \varepsilon \sum_i \mathbf{S}_i \cdot \mathbf{S}_{i+1} . \quad (6)$$

Using the spectrum of single mode approximation (SMA) excitations, it is possible to derive an approximate perturbation theory in the difference $H - H_{\text{AKLT}}$. (Note that SMA was employed previously to elucidate the relation between valence bond states (VBS) and the Laughlin state [47].) The idea goes back to unpublished work of Haldane, and was later elucidated in Ref. [48]. One proceeds by idealizing the triplet SMA levels as bosonic excitations, and asserting the approximate operator correspondence

$$S_k^\alpha \approx \sqrt{s(k)} (b_{k,\alpha}^\dagger + b_{-k,\alpha}), \quad (7)$$

where $s(k) = \langle \Psi_0 | S_k^\alpha S_{-k}^\alpha | \Psi_0 \rangle$ (no sum on α) is the static structure factor. The bosonic form of the perturbed Hamiltonian in (6) is then

$$H_{\text{bos}} = \sum_{k,\alpha} \left[\omega(k) b_{k,\alpha}^\dagger b_{k,\alpha} + \varepsilon s(k) \cos k (b_{k,\alpha}^\dagger + b_{-k,\alpha})(b_{-k,\alpha}^\dagger + b_{k,\alpha}) \right], \quad (8)$$

where the structure factor and SMA dispersion were computed in Ref. [47] and found to be $s(k) = 2(1 - \cos k)/(5 + 3 \cos k)$ and $\omega(k) = \frac{5}{27}(5 + 3 \cos k)$. Solving H_{bos} by a Bogoliubov transformation, one obtains the renormalized structure factor

$$\tilde{s}(k) = \left(\frac{\omega(k)}{\omega(k) + 2\varepsilon \Delta(k)} \right)^{1/2} s(k), \quad (9)$$

where $\Delta(k) = 2 s(k) \cos k$. The corresponding spin wavefunction is then given by

$$|\tilde{\Psi}_0\rangle = \exp \left(- \sum_k \left(\frac{1}{\tilde{s}(k)} - \frac{1}{s(k)} \right) S_k^\alpha S_{-k}^\alpha \right) |\Psi_0\rangle, \quad (10)$$

where $|\Psi_0\rangle$ denotes the AKLT ground state. Expanding to leading power in ε , we have

$$|\tilde{\Psi}_0\rangle = \left\{ 1 - \frac{\varepsilon}{2} \sum_{n,n'} K_{nn'} S_n^\alpha S_{n'}^\alpha + \mathcal{O}(\varepsilon^2) \right\} |\Psi_0\rangle, \quad (11)$$

where the kernel $K_{nn'}$ is the Fourier transform of $2\Delta(k)/\omega(k)s(k) = 4 \cos k/\omega(k)$, and is given by the expression ($j := n - n'$)

$$K(j) = \int_0^{2\pi} \frac{dk}{2\pi} \frac{4 \cos k}{\omega(k)} e^{ikj} = \frac{36}{5} \varepsilon \delta_{j,0} - 9 \varepsilon \left(-\frac{1}{3} \right)^j. \quad (12)$$

The expression for $|\tilde{\Psi}_0\rangle$ has a clear correspondence with first order perturbation theory, wherein

$$|\Psi'_0\rangle = |\Psi_0\rangle - \sum_n \frac{1}{E_n} |n\rangle \langle n| 2\varepsilon \sum_k \cos(k) S_k^\alpha S_{-k}^\alpha |\Psi_0\rangle, \quad (13)$$

if we approximate $|n\rangle \approx s(k)^{-1} (1 - |\Psi_0\rangle \langle \Psi_0|) S_k^\alpha S_{-k}^\alpha |\Psi_0\rangle$, and $E_n \approx \omega(k)$.

6.3. Operator product expansion of the SMA wave function

Defining the operator-valued matrix,

$$M(j) = \begin{pmatrix} 1 & S_j^x & S_j^y & S_j^z & 0 \\ 0 & e^{-\alpha} & 0 & 0 & S_j^x \\ 0 & 0 & e^{-\alpha} & 0 & S_j^y \\ 0 & 0 & 0 & e^{-\alpha} & S_j^z \\ 0 & 0 & 0 & 0 & 1 \end{pmatrix}, \quad (14)$$

and the vectors

$$\langle L| = \begin{pmatrix} -3\varepsilon & 0 & 0 & 0 & 1 \end{pmatrix}, \quad |R\rangle = \begin{pmatrix} 0 \\ 0 \\ 0 \\ 0 \\ 1 \end{pmatrix}, \quad (15)$$

we have the matrix product operator (MPO) expression,

$$\langle L| M(1) \cdots M(N) |R\rangle = 1 + \sum_{n < n'} K(n - n') S_n^\alpha S_{n'}^\alpha. \quad (16)$$

If the AKLT state is written in matrix product form as

$$|\Psi_0\rangle = \langle \mathcal{L}| \mathcal{A}^{m_1} \cdots \mathcal{A}^{m_N} |\mathcal{R}\rangle |m_1, \dots, m_N\rangle, \quad (17)$$

where $\langle \mathcal{L}|$ and $\langle \mathcal{R}|$ are vectors which passivate the end sites $n = 1$ and $n = N$, rendering them $S = \frac{1}{2}$, then the SMA state is a MPS with

$$|\Psi\rangle = \langle L| A^{m_1} \cdots A^{m_N} |R\rangle |m_1, \dots, m_N\rangle, \quad (18)$$

where

$$A_{i,i'}^m = \langle m| M_{aa'} |m'\rangle \mathcal{A}_{\mu,\mu'}^{m'}, \quad (19)$$

and $i = (a, \mu)$ is a composite index. In our example, a runs from 1 to 5, μ from 1 to 2, and m from 1 to 3. Thus, i runs from 1 to $5 \cdot 2 = 10$. Similarly, $|L\rangle = |L\rangle \otimes |\mathcal{L}\rangle$, etc. The fact that $A_{i,i'}^m$ is of rank ten means that there must be ten entanglement levels.

More frequent than a double cut of a finite size bipartition, the single cut associated with a semi-infinite partition has been employed to identify the symmetry-protected topological character of the Haldane phase [11]. The latter is simulated for small finite size by passivating the dangling spins in an OBC geometry (Fig. 1b) and choosing the $S_{\text{tot}}^z = \pm 1$ sector. Combining the valence-bond picture (see Fig. 9) and the framework of SMA, we will demonstrate that the ES in the Haldane phase must be two-fold (or, in general, even-numbered) degenerate.

Suppose we partition the chain such that sites $j \in \{1, 2, \dots, N_A\}$ are in subsystem A and the remaining sites are in subsystem B. It follows that we may write

$$|\Psi_{\text{SMA}}\rangle = |\Psi_0\rangle + |\Psi_A\rangle + |\Psi_B\rangle + |\Psi_{AB}\rangle, \quad (20)$$

where $|\Psi_A\rangle$ includes contributions for $n < n' \leq N_A$, $|\Psi_B\rangle$ includes contributions for $N_A < n < n'$, and $|\Psi_{AB}\rangle$ includes contributions for $n < N_A < n'$ (Eq. 11).

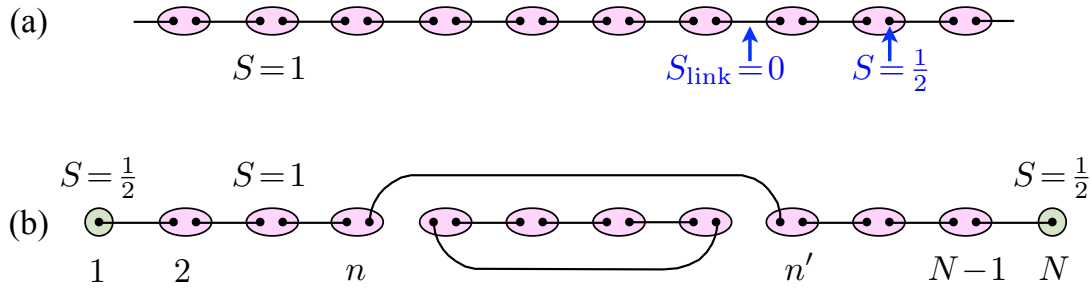


Figure 9. (a) $S = 1$ AKLT state; each lattice site (pink ellipses) is given by the symmetrization of two virtual spin- $\frac{1}{2}$ degrees of freedom. One of them is antisymmetrized in the singlet bond to the left while the other is antisymmetrized in a singlet bond to the right. (b) Visualization of the state $|nn'\rangle$ within the SMA framework for the AKLT chain with passivated $S = \frac{1}{2}$ ends.

We may then write the density matrix $\rho = |\Psi\rangle\langle\Psi|$ as $\rho = \rho_0 + \rho_A + \rho_B + \rho_{AB}$, where $\rho_A = |\Psi_0\rangle\langle\Psi_A| + |\Psi_A\rangle\langle\Psi_0|$, $\rho_B = |\Psi_0\rangle\langle\Psi_B| + |\Psi_B\rangle\langle\Psi_0|$, and $\rho_{AB} = |\Psi_0\rangle\langle\Psi_{AB}| + |\Psi_{AB}\rangle\langle\Psi_0|$. We now perform the partial trace over the B subsystem. For ρ_0 , ρ_A , and ρ_B , this results in one link being severed by the entanglement cut. There are then exactly two entanglement eigenstates in each case (*i.e.*, a doublet). For ρ_{AB} , three links are severed (see Fig. 9), resulting in two doublets and one quadruplet entanglement levels. Assuming that the doublets are linearly independent, we find three linearly independent doublets and one quadruplet, resulting in ten entanglement levels, as previously deduced. The upshot of this analysis is that one predicts the appearance of doublets and quadruplets, but nothing else. Here we recover the two-fold degeneracy (or, more generally, even-number degeneracy) of the ES for the Haldane phase [11]. If we allow for higher processes and go beyond the linearized SMA version considered here, we will generate higher-order links as compared to $|nn'\rangle$. Still only configurations are generated where the real space cut intersects an *odd* number of links. Therefore the ES will remain even-numbered degenerate.

The double degeneracy of the ES for a single cut in the Haldane phase clearly distinguishes the Haldane phase from the dimer phase. While the SMA picture can explain the two-fold degeneracy in the ES, one might naively expect that breaking of $SU(2)$ symmetry would lift these degeneracies. This is, however, not true. As shown in Ref. [11], the Haldane phase is *protected* by time-reversal, bond-inversion, and dihedral symmetries. One needs to break all these symmetries in order to loose the degeneracy of the entanglement spectrum. In the meantime it is well-established that the Haldane phase is an SPT phase [49]. The double degeneracy in the entanglement spectrum is a hallmark for such a SPT phase when only a single cut is considered, as just explained. When PBCs are imposed and two cuts are present, multiplets stemming from the two cuts decompose into multiplets such as singlet, triplet etc. The simplest example is the pure AKLT state where a doublet on both cuts is present resulting in one singlet and

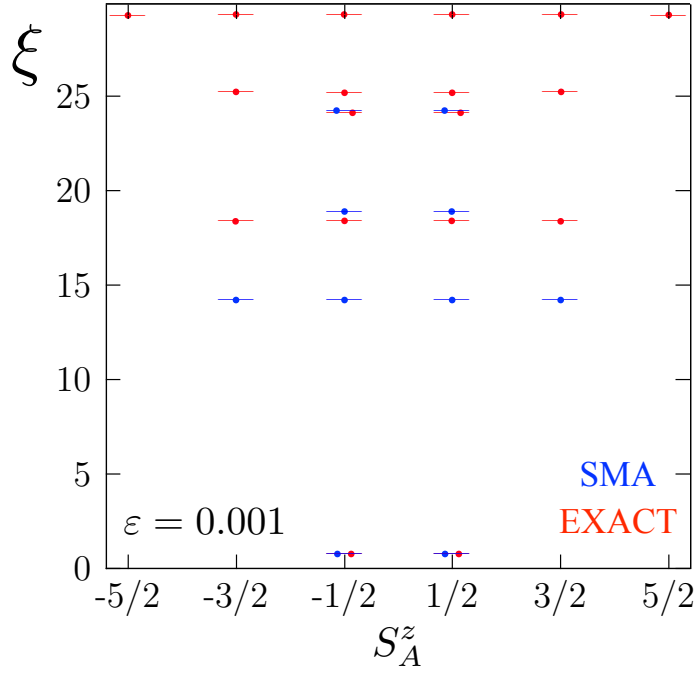


Figure 10. Comparison of the SMA-corrected ground state entanglement spectrum (leading order in ε , blue) (Eq. 11) and the exact ground state entanglement spectrum for a single cut in a $N = 12$ site chain of the Hamiltonian in Eq. 6 (red). All entanglement levels are even-fold degenerate in both cases. Since we mimic the single cut by imposing OBC and $S_{\text{tot}}^z = 1$, exact $\text{SU}(2)$ symmetry in the ES is lost, but is still approximately present.

one triplet level. There is no non-trivial even/odd degeneracy constraint anymore.

6.4. Comparison of SMA predictions with numerical results

We test the SMA method quantitatively by comparing the entanglement spectrum of the SMA-modified ground state wavefunction with that of the exact ground state. We first consider an open chain with $N = 12$ sites and make a single entanglement cut which divides the system into two half-chains. The end spins are passivated by fixing $S_{\text{tot}}^z = 1$. In Fig. 10 we show both SMA (blue) and exact ES (red) for $\varepsilon = 0.001$. The lowest-lying doublet, the entanglement ground state, is followed by a quadruplet and another doublet. The SMA state entanglement level multiplet structure is as predicted above (*i.e.* ten levels in total), but deviates noticeably from the exact result for entanglement levels above the lowest doublet. One reason is that the SMA-corrected ground state is of the form $\exp\left(\sum_{j=1}^{\infty} \varepsilon^j \hat{\mathcal{Q}}_j\right) |\Psi_0\rangle$, where $\{\hat{\mathcal{Q}}_j\}$ are operators which scale extensively with system size. Hence an expansion of the exponential is really an expansion in powers of $N\varepsilon$. We can do a little better by expanding the SMA-corrected ground state wavefunction to second order, writing

$$|\tilde{\Psi}_0\rangle = \left\{ 1 - \frac{\varepsilon}{2} \mathcal{M}^{(1)} + \frac{\varepsilon^2}{8} \mathcal{M}^{(2)} + \frac{\varepsilon^2}{8} (\mathcal{M}^{(1)})^2 + \mathcal{O}(\varepsilon^3) \right\} |\Psi_0\rangle, \quad (21)$$

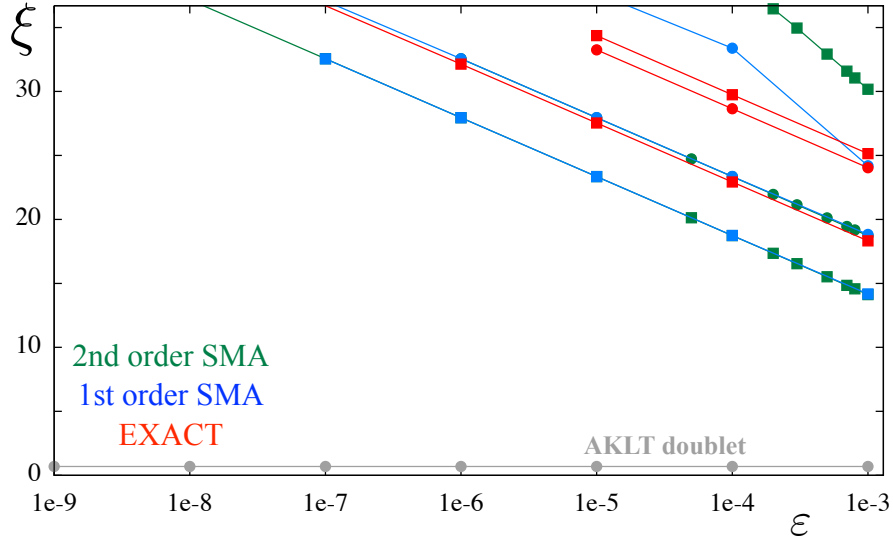


Figure 11. Evolution of entanglement spectra for an $N = 12$ site chain of Eq. (6) as a function of ε . A single cut is used with $S_{\text{tot}}^z = 1$ enforced to passivate the two end spins. Comparisons of the exact ground state (red) with first (blue) and second (green) order SMA-corrected ground states are shown. All states exhibit the characteristic AKLT doublet whose ξ level does not change with ε within machine precision. All doublets are depicted by full circles and the quartets by full squares. The lowest entanglement levels above the AKLT doublet are hardly affected by moving from 1st to 2nd order SMA. The quantitative deviation of the SMA levels from the exact levels is small in terms of absolute entanglement weight, given the high values of ξ .

where $\mathcal{M}^{(r)} = \sum_k \frac{1}{s(k)} \left(\frac{2s(k) \cos k}{\omega(k)} \right)^r S_k^\alpha S_{-k}^\alpha = \sum_{n,n'} K_{n-n'}^{(r)} S_n^\alpha S_{n'}^\alpha$, with $K_j^{(1)} \equiv K(j)$ in Eq. 12 above, and

$$K_j^{(2)} = -\frac{864}{25} \delta_{j,0} + \frac{27}{200} \left(-\frac{1}{3} \right)^j \cdot (527 - 180j + 400j^2). \quad (22)$$

In Fig. 11 we compare the low-lying entanglement levels related to Eq. 6 for the exact ground state as well as the first and second order SMA results, as a function of ε . We find that the ES is strongly affected for levels above the lowest eight states arranged in the doublet, quadruplet, doublet order. Due to the second order contribution, the sequence of entanglement levels (d=doublet and q=quartet) changes from d-q-d-d for the first order SMA to d-q-d-q, which matches the exact sequence. Still, the second order contribution modifies the entanglement profile only marginally. The fact that there is still only a rough quantitative correspondence in ξ between the higher lying entanglement levels for the SMA-corrected and exact ground state indicates that the source of the disagreement lies in the approximate nature of the Bogoliubov-SMA approach itself, rather than the passivation of the end spins by projecting onto $S_{\text{tot}}^z = 1$, or the finite order expansion in $N\varepsilon$.

7. CONCLUSION

We have employed finite size ground state bipartitions to analyze the entanglement structure of isotropic spin-1 chains. The isotropic bilinear-biquadratic model allowed us to interpret many hallmark features of quantum spin chains from the viewpoint of entanglement. We investigated spontaneous breaking of translation symmetry in the dimerized phase and spin rotation symmetry in the ferromagnetic domain. Both phenomena can be unambiguously identified from entanglement just by analyzing a single small system size. Furthermore, we have shown how enhanced internal $SU(3)$ symmetry affects not only the degeneracy structure of entanglement spectra similar to Hamiltonian spectra, but also the pronounced extensive amount of zero weight entanglement levels as seen for the Uimin-Lai-Sutherland point. This spectral distribution feature of entanglement approximately persists for the whole quadrupolar phase. Finally, the SPT character of the Haldane phase is precisely resolved by entanglement spectra. We have elucidated the correspondence between a boundary Hamiltonian spectrum and the entanglement spectrum of the associated ground state for periodic boundary conditions. In particular, we have identified the notion of the entanglement gap to hold in the thermodynamic limit. For the single mode approximation of the perturbed AKLT state and the operator product expansion derived from there, entanglement spectra allowed us to obtain a complementary view on the accuracy of this approach.

Our study strongly supports the view that the analysis of entanglement spectra of one-dimensional quantum systems provides insight which leverages the analysis of relatively small finite size systems, and will thereby constitute a preferable choice when large scale calculations are either not feasible or unavailable.

Acknowledgments

We thank F. Pollmann, P. Schmitteckert, and U. Schollwöck for valuable discussions. This work has been supported by the ERC Starting Grant ERC-StG-Thomale-TOPOLECTRICS-336012. SR is supported by the DFG through FOR 960 and by the Helmholtz association through VI-521. BAB acknowledges support from NSF CAREER DMR-0952428, ONR-N00014-11-1-0635, MURI-130-6082, DARPA under SPAWAR Grant No.: N66001-11-1-4110, the Packard Foundation, and a Keck grant.

Appendix A. Derivation of enhanced $SU(3)$ symmetry models

For completeness, we elaborate on the points of (1) where the Spin 1 $SO(3)$ model exhibits enhanced internal $SU(3)$ symmetry. We follow the notation of [50], and prove below that both Hamiltonians $\theta = \pi/4$ and $\theta = 3\pi/2$ of (1) possess an enlarged $SU(3)$ symmetry. Since both models exhibit $SU(3)$ singlet ground states, the same argument of for $SU(2)$ in Section 2 applies and as such, the internal symmetry operator generating the

block diagonal form of the entanglement spectrum is given by $[T^a, \rho_A] = 0$, $T^a = \sum_i T_i^a$, where T^a are the generators in $\mathfrak{sl}(3)$. This yields $SU(3)$ multiplets in the entanglement spectrum.

Appendix A.1. $SU(3)$ Heisenberg model

To prove the $SU(3)$ invariance at the Hamiltonian level, we develop an *a posteriori* perspective and consider the $SU(3)$ Heisenberg Hamilton operator

$$H = \sum_i^N T_i^a T_{i+1}^a, \quad (\text{A.1})$$

with implicit summation over $a = 1, \dots, 8$. We label the representation states of the fundamental representation rep. 3 by the colors blue (b), red (r), and green (g) (quarks). We will also treat the non-equivalent representation $\bar{\mathbf{3}}$ later, *i.e.*, where the states possess the complementary colours yellow (y), cyan (c), and magenta (m) (anti-quarks). Labelling the Gell-Mann representation by λ^a in order not to confuse it with the generators T , the action on the fundamental representation 3 is given by

$$\begin{aligned} \lambda^1 &= \begin{pmatrix} 0 & 1 & 0 \\ 1 & 0 & 0 \\ 0 & 0 & 0 \end{pmatrix}, & \lambda^2 &= \begin{pmatrix} 0 & -i & 0 \\ i & 0 & 0 \\ 0 & 0 & 0 \end{pmatrix}, & \lambda^3 &= \begin{pmatrix} 1 & 0 & 0 \\ 0 & -1 & 0 \\ 0 & 0 & 0 \end{pmatrix}, \\ \lambda^4 &= \begin{pmatrix} 0 & 0 & 1 \\ 0 & 0 & 0 \\ 1 & 0 & 0 \end{pmatrix}, & \lambda^5 &= \begin{pmatrix} 0 & 0 & -i \\ 0 & 0 & 0 \\ i & 0 & 0 \end{pmatrix}, & \lambda^6 &= \begin{pmatrix} 0 & 0 & 0 \\ 0 & 0 & 1 \\ 0 & 1 & 0 \end{pmatrix}, \\ \lambda^7 &= \begin{pmatrix} 0 & 0 & 0 \\ 0 & 0 & -i \\ 0 & i & 0 \end{pmatrix}, & \lambda^8 &= \frac{1}{\sqrt{3}} \begin{pmatrix} 1 & 0 & 0 \\ 0 & 1 & 0 \\ 0 & 0 & -2 \end{pmatrix}. \end{aligned} \quad (\text{A.2})$$

Their normalization is chosen to be

$$\text{tr}(\lambda^a \lambda^b) = 2\delta_{ab}.$$

The Gell-Mann matrices form an orthogonal basis of \mathfrak{sl}_3 , the Lie algebra of $SU(3)$, and satisfy the commutation relations

$$[\lambda^a, \lambda^b] = 2if^{abc}\lambda^c. \quad (\text{A.3})$$

The structure constants f^{abc} are totally antisymmetric and obey Jacobi's identity

$$f^{abc}f^{cde} + f^{bdc}f^{cae} + f^{dac}f^{cbe} = 0. \quad (\text{A.4})$$

All non-vanishing structure constants are obtained by permutations of the indices from

$$\begin{aligned} f^{123} &= 1 \\ f^{147} &= f^{246} = f^{257} = f^{345} = \frac{1}{2} \\ f^{156} &= f^{367} = -\frac{1}{2} \\ f^{458} &= f^{678} = \frac{\sqrt{3}}{2}. \end{aligned} \quad (\text{A.5})$$

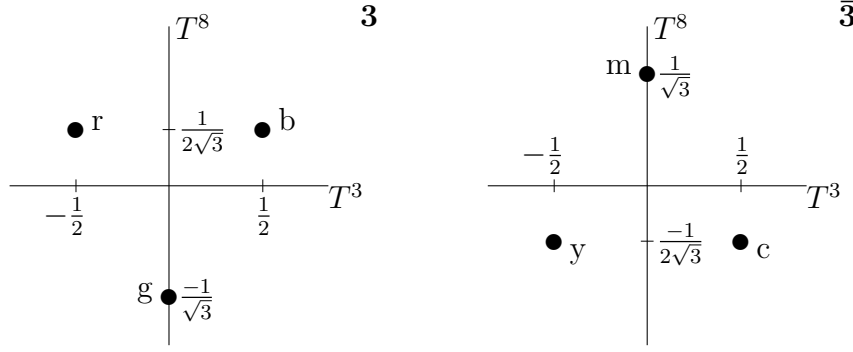


Figure A1. Weight diagrams of the three-dimensional representations of $SU(3)$. T^3 and T^8 are the diagonal generators.

The Gell-Mann matrices also close with respect to the anticommutator:

$$\{\lambda_a, \lambda_b\} = \frac{4}{3}\delta_{ab} + d_{abc}\lambda_c, \quad (\text{A.6})$$

with the fully symmetric structure constants

$$\begin{aligned} d^{118} = d^{228} = d^{338} = -d^{888} &= \frac{2}{\sqrt{3}} \\ d^{448} = d^{558} = d^{668} = d^{778} &= -\frac{1}{\sqrt{3}} \\ d^{146} = d^{157} = -d^{247} = d^{256} = d^{344} = d^{355} = -d^{366} = -d^{377} &= 1 \end{aligned} \quad (\text{A.7})$$

Appendix A.2. $SU(3)$ symmetry at $\theta = \pi/4$

We now specify the Hilbert space the Hamiltonian (A.1) acts on. Considering $3 \times 3 \times 3 \times 3 \times 3 \dots$, we can thus write the Hamiltonian more specifically in terms of the λ s:

$$H = \sum_i^N \lambda_i^a \lambda_{i+1}^a. \quad (\text{A.8})$$

Next, note that the fundamental representation of the Lie algebra $\mathfrak{o}(3)$ relates to the $SU(2)$ spin 1 operators, because the $SU(2)$ is locally isomorphic to $O(3)$ and the representations have the same dimensionality. As such, we can readily identify the $O(3)$ type operators of the Gell Mann matrices. For s_l , $l = 1, 2, 3$ and spin 1 operators, this yields

$$s_1 = \lambda_7, \quad s_2 = -\lambda_5, \quad s_3 = \lambda_2, \quad (\text{A.9})$$

enabling us to write the spin 1 bilinear terms in terms of λ s. The same can be done for the biquadratic terms, exploiting anti-commutation and commutation relations of the Gell-Mann matrices λ [50]. Accordingly, the Hamiltonian part $\sum_i^N \mathbf{S}_i \cdot \mathbf{S}_{i+1}$ is readily identified via $\lambda_2 = S_3$, $\lambda_5 = -S_2$, $\lambda_7 = S_1$ and yields

$$\sum_i^N \mathbf{S}_i \cdot \mathbf{S}_{i+1} = \sum_i^N \sum_{a=2,5,7} \lambda_i^a \lambda_{i+1}^a. \quad (\text{A.10})$$

In turn, the biquadratic Hamiltonian part $H_{bq} = (\mathbf{S}_i \cdot \mathbf{S}_{i+1})^2$ is rewritten as

$$H_{bq} = (\lambda_i^2 \lambda_{i+1}^2)^2 + (\lambda_i^5 \lambda_{i+1}^5)^2 + (\lambda_i^7 \lambda_{i+1}^7)^2 \quad (\text{A.11})$$

$$+ \lambda_i^2 \lambda_i^5 \lambda_{i+1}^2 \lambda_{i+1}^5 + [2 \leftrightarrow 5] \quad (\text{A.12})$$

$$+ \lambda_i^2 \lambda_i^7 \lambda_{i+1}^2 \lambda_{i+1}^7 + [2 \leftrightarrow 7] \quad (\text{A.13})$$

$$+ \lambda_i^5 \lambda_i^7 \lambda_{i+1}^5 \lambda_{i+1}^7 + [5 \leftrightarrow 7] \quad (\text{A.14})$$

Whenever spatial indices are suppressed in the following, we assume that multiple powers of λ act on the same site. To calculate Eq. A.11, we make use of A.6 and find $(\lambda^2)^2 = \frac{1}{2}(\frac{4}{3} + \frac{2}{\sqrt{3}}\lambda^8)$, $(\lambda^5)^2 = \frac{1}{2}(\frac{4}{3} - \frac{1}{\sqrt{3}}\lambda^8 + \lambda^3)$, $(\lambda^7)^2 = \frac{1}{2}(\frac{4}{3} - \frac{1}{\sqrt{3}}\lambda^8 - \lambda^3)$. Factoring everything out, Eq. A.11 becomes $\frac{1}{2}\lambda_i^8 \lambda_{i+1}^8 + \frac{1}{2}\lambda_i^3 \lambda_{i+1}^3 + \frac{4}{3}$. The latter constant we can discard as a global constant factor, the rest are just the bilinears of the Casimirs. The subsequent lines A.12, A.13, and A.14, can be calculated analogously, so we will only show Eq. A.12. Trivial algebra yields the (anti-)symmetrized form $\lambda_i^2 \lambda_i^5 \lambda_{i+1}^2 \lambda_{i+1}^5 + [2 \leftrightarrow 5] = \frac{1}{2}[\lambda^2, \lambda^5]_i \{\lambda^2, \lambda^5\}_{i+1} + \frac{1}{2}[\lambda^5, \lambda^2]_i \{\lambda^2, \lambda^5\}_{i+1} + \frac{1}{2}[\lambda^2, \lambda^5]_i [\lambda^2, \lambda^5]_{i+1} + \frac{1}{2}\{\lambda^2, \lambda^5\}_i \{\lambda^2, \lambda^5\}_{i+1} = \frac{1}{2}[\lambda^2, \lambda^5]_i [\lambda^2, \lambda^5]_{i+1} + \frac{1}{2}\{\lambda^2, \lambda^5\}_i \{\lambda^2, \lambda^5\}_{i+1}$. Now, we can make use of (A.3) and (A.6) to find $[\lambda^2, \lambda^5] = i\lambda^7$ and $\{\lambda^2, \lambda^5\} = \lambda_6$, such that the final result is $\frac{1}{2}(\lambda_i^6 \lambda_{i+1}^6 - \lambda_i^7 \lambda_{i+1}^7)$. We find

$$\sum_i^N (\mathbf{S}_i \cdot \mathbf{S}_{i+1})^2 = \frac{1}{2} \sum_i^N \left(\sum_{a=1,3,4,6,8} \lambda_i^a \lambda_{i+1}^a - \sum_{a=2,5,7} \lambda_i^a \lambda_{i+1}^a \right). \quad (\text{A.15})$$

Adding (A.10) and (A.15) yields the Hamiltonian to be symmetric with respect to the Gell-Mann index a , i.e. to SU(3).

Appendix A.3. SU(3) symmetry at $\theta = 3\pi/2$

Again starting from A.1, we consider the Hilbert space spanned by $3 \times \bar{3} \times 3 \times \bar{3} \dots$. This has consequences for the SU(3) Hamiltonian, as the imaginary-valued λ 's for $a = 2, 5, 7$ acting on $\bar{3}$ yield one minus sign due to complex conjugation. Performing the same algebra as before, we find the purely biquadratic Hamiltonian (A.15) to be SU(3) invariant if acting on the modified Hilbert space, anticipating a doubling of the unit cell along the dimerized ground state at $\theta = 3\pi/2$.

Appendix B. Scaling of the entanglement gap

As discussed in Sec. 5, the even-odd behavior of the ES with respect to entanglement cuts corresponding to even and odd subsystem lengths is reminiscent of translation symmetry breaking in the dimerized phase. Different, even though similar even-odd effects, however, can also be observed under different circumstances such as for a gapless spin- $\frac{1}{2}$ Heisenberg chain. For the even-odd discrepancy to provide substantiated information, it is hence important to distinguish a gapped from a gapless phase. It turns out that the scaling of the entanglement gap clearly distinguishes both cases (we restrict the discussion to half-chain cuts). We define the entanglement gap as the gap between the entanglement levels belonging to the entanglement ground state and

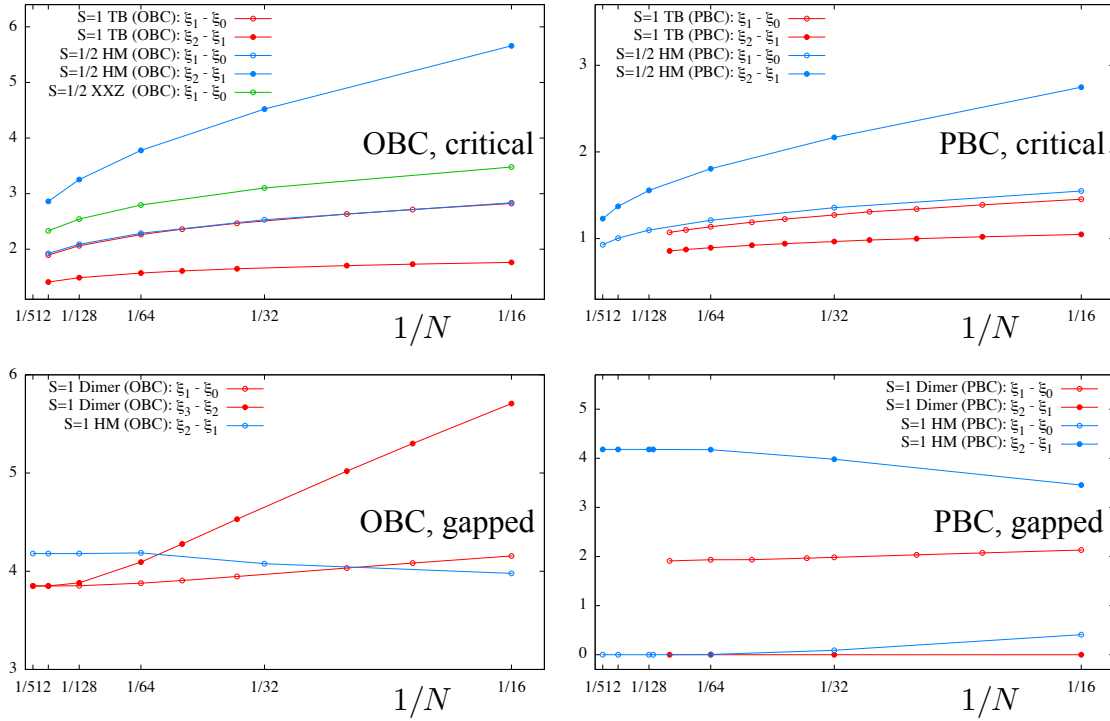


Figure B1. (Color online) Scaling of the entanglement gap for gapped and gapless models for OBC and PBC obtained within DMRG. While the gapless models exhibit non-trivial spectral flow for large system sizes (see text for details), the gapped models show saturation of the entanglement gap.

higher-lying entanglement levels. For instance, for spin 1 Heisenberg chain with PBC the entanglement gap is above the lowest singlet and triplet; for the spin- $\frac{1}{2}$ Heisenberg chain, we consider the gap above the single lowest singlet state. Fig. B1 shows examples for gapped and gapless models. Plots on the left (right) correspond to OBC (PBC). The spin 1 Takhtajan-Babujian (TB) model ($\theta = 7\pi/4$), the spin- $\frac{1}{2}$ Heisenberg chain, and the spin- $\frac{1}{2}$ XXZ chain with Ising anisotropy $\Delta = 0.5$ are examples for the gapless case, the spin 1 Heisenberg chain ($\theta = 0$) and the dimer model with $\theta = 3\pi/2$ are examples for the gapped case. For the spin- $\frac{1}{2}$ Heisenberg model and the spin 1 TB model, both $\xi_1 - \xi_0$ and $\xi_2 - \xi_1$ are shown. The characteristic scaling behavior vs. $1/N$ agrees with the prediction of Calabrese and Lefevre [51, 52]. For gapped models, we find that the entanglement gap already saturates for rather small systems sizes ($N = 30$ for OBC, $N = 60$ for PBC), supporting the existence of an entanglement gap in the thermodynamic limit.

- [1] L. Amico, R. Fazio, A. Osterloh, and V. Vedral, Rev. Mod. Phys. **80**, 517 (2008).
- [2] H. Li and F. D. M. Haldane, Phys. Rev. Lett. **101**, 010504 (2008).
- [3] R. Thomale, A. Sterdyniak, N. Regnault, and B. A. Bernevig, Phys. Rev. Lett. **104**, 180502 (2010).
- [4] J. Dubail and N. Read, Phys. Rev. Lett. **107**, 157001 (2011).
- [5] A. Sterdyniak, N. Regnault, and B. A. Bernevig, Phys. Rev. Lett. **106**, 100405 (2011).
- [6] A. Chandran, M. Hermanns, N. Regnault, and B. A. Bernevig, Phys. Rev. B **84**, 205136 (2011).

- [7] X.-L. Qi, H. Katsura, and A. W. W. Ludwig, Phys. Rev. Lett. **108**, 196402 (2012).
- [8] A. M. Turner, Y. Zhang, and A. Vishwanath, Phys. Rev. B **82**, 241102 (2010).
- [9] R. Thomale, B. Estienne, N. Regnault, and B. A. Bernevig, Phys. Rev. B **84**, 045127 (2011).
- [10] M. J. Gilbert, B. A. Bernevig, and T. L. Hughes, Phys. Rev. B **86**, 041401 (2012).
- [11] F. Pollmann, A. M. Turner, E. Berg, and M. Oshikawa, Phys. Rev. B **81**, 064439 (2010).
- [12] L. Fidkowski, Phys. Rev. Lett. **104**, 130502 (2010).
- [13] A. Chandran, V. Khemani, and S. Sondhi, Phys. Rev. Lett. **113**, 060501 (2014).
- [14] H. F. Song, S. Rachel, C. Flindt, I. Klich, N. Laflorencie, and K. Le Hur, Phys. Rev. B **85**, 035409 (2012).
- [15] P. Calabrese and A. Lefevre, Phys. Rev. A **78**, 032329 (2008).
- [16] P. Calabrese and J. Cardy, J. Stat. Mech. P06002 (2004).
- [17] A. M. Läuchli, arXiv:1303.0741.
- [18] L. Fidkowski and A. Kitaev, Phys. Rev. B **83**, 075103 (2011).
- [19] G. Fáth and J. Sólyom, Phys. Rev. B **44**, 11836 (1991).
- [20] C. Itoi and M.-H. Kato, Phys. Rev. B **55**, 8295 (1997).
- [21] A. Läuchli, G. Schmid, and S. Trebst, Phys. Rev. B **74**, 144426 (2006).
- [22] G. V. Uimin, JETP Lett. **12**, 225 (1970).
- [23] C. K. Lai, J. Math. Phys. **15**, 1675 (1974).
- [24] B. Sutherland, Phys. Rev. B **12**, 3795 (1975).
- [25] F. D. M. Haldane, Phys. Rev. Lett. **50**, 1153 (1983).
- [26] I. Affleck, T. Kennedy, E. H. Lieb, and H. Tasaki, Phys. Rev. Lett. **59**, 799 (1987).
- [27] S. R. White, Phys. Rev. Lett. **69**, 2863 (1992).
- [28] U. Schollwöck, T. Jolicœur, and T. Garel, Phys. Rev. B **53**, 3304 (1996).
- [29] L. Takhtajan, Phys. Lett. A **87**, 479 (1982).
- [30] H. Babujian, Phys. Lett. A **90**, 479 (1982).
- [31] I. Affleck and F. D. M. Haldane, Phys. Rev. B **36**, 5291 (1987).
- [32] K. Buchta, G. Fáth, O. Legeza, and J. Sólyom, Phys. Rev. B **72**, 054433 (2005).
- [33] S. Hu, A. M. Turner, K. Penc, and F. Pollmann, Phys. Rev. Lett. **113**, 027202 (2014).
- [34] R. Thomale, D. P. Arovas, and B. A. Bernevig, Phys. Rev. Lett. **105**, 116805 (2010).
- [35] R. Lundgren, J. Blair, M. Greiter, A. Läuchli, G. A. Fiete, and R. Thomale, Phys. Rev. Lett. **113**, 256404 (2014).
- [36] R. Lundgren, arXiv:1412.8612.
- [37] D. Poilblanc, Phys. Rev. Lett. **105**, 077202 (2010).
- [38] R. Lundgren, V. Chua, and G. A. Fiete, Phys. Rev. B **86**, 224422 (2012).
- [39] E. H. Lieb, T. Schultz, and D. Mattis, Ann. Phys. **16**, 407 (1961).
- [40] S. Rachel, R. Thomale, M. Führinger, P. Schmitteckert, and M. Greiter, Phys. Rev. B **80**, 180420 (2009).
- [41] M. Führinger, S. Rachel, R. Thomale, M. Greiter, and P. Schmitteckert, Ann. Phys. (Berlin) **17**, 922 (2008).
- [42] M. N. Barber and M. T. Batchelor, Phys. Rev. B **40**, 4621 (1989).
- [43] Y. Xian, J. Phys. Lett. A **183**, 437 (1993).
- [44] A. Klümper, Eur. Phys. Lett. **9**, 815 (1989).
- [45] V. Alba, M. Haque, and A. M. Läuchli, Phys. Rev. Lett. **108**, 227201 (2012).
- [46] R. Orús, T.-C. Wei, and H.-H. Tu, Phys. Rev. B **84**, 064409 (2011).
- [47] D. P. Arovas, A. Auerbach, and F. D. M. Haldane, Phys. Rev. Lett. **60**, 531 (1988).
- [48] D. Arovas and S. Girvin, in *Recent Progress in Many-Body Theories*, edited by T. Ainsworth, C. Campbell, B. Clements, and E. Krotscheck (Plenum, New York, 1992), pp. 315–344.
- [49] X. Chen, Z.-C. Gu, Z.-X. Liu, and X.-G. Wen, Science **338**, 1604 (2012).
- [50] K.-H. Mütter, Z. Phys. B **96**, 105 (1994).
- [51] P. Calabrese and A. Lefevre, Phys. Rev. A **78**, 032329 (2008).
- [52] N. Laflorencie and S. Rachel, J. Stat. Mech. **2014**, P11013 (2014).